CHAPTER X *TEM TECHNIQUES FOR CHARACTERIZING DISLOCATIONS*

10.1 Transmission Electron Microscopy

Transmission Electron Microscopy (TEM) is a powerful tool in the field of materials physics, particularly for characterizing crystal defects such as dislocations. Dislocations are line defects within a crystal that can drastically alter a material's properties, including its mechanical strength and electrical behavior. The first in-situ measurements of dislocations and dislocation motion in a Transmission Electron Microscope (TEM) were groundbreaking because they provided direct, real-time visualization of these phenomena at the atomic scale. Early works, such as those by Hirsch, Bollmann, and others, utilized darkfield and brightfield imaging modes to identify and observe dislocations. The resolution was limited, but they could still capture dislocation networks and estimate their density. This capability enables researchers to observe how dislocations, line defects in the crystal structure, behave under various conditions, such as mechanical stress, thermal activation, and other environmental factors.

The development of weak-beam darkfield (WBDF) imaging further improved the ability to visualize and analyze dislocations by enhancing contrast. This technique helps researchers study the fine structure of dislocations and understand their core configurations and motion mechanisms. Properly implementing the WBDF and analyzing these defects requires a deep understanding of diffraction-contrast mechanisms, which can be described by the Howie-Whelan equations. As such, this chapter will introduce the Howie-Whelan equations and explain how they are used to characterize a dislocation's line direction and Burgers vector using brightfield, darkfield, and weak-beam imaging techniques.

In addition to these diffraction contrast imaging techniques, this chapter will discuss modern TEM techniques, such as aberration-corrected high-resolution TEM (HRTEM), scanning TEM (STEM), and in-situ mechanical testing, which have enabled even more precise and detailed observations of dislocation behavior. These methods allow scientists to analyze dislocations at near-atomic resolution, track their motion under varying environmental conditions, and measure their interactions with other microstructural features.

10.1.1 A Brief History and Background

The fifth Solvay Conference on Physics, held in 1927 and attended by some of the most prominent minds, ushered in a new era of science and quantum mechanics. The conference title was simple: Electrons and Photons. One of those famous attendees was the French physicist Louis de Broglie. He postulated that electrons exhibit wave behavior, a fundamental tenet of quantum mechanics that underlies wave-particle duality. However, these ideas remained controversial and were neither widely adopted nor proven in the 1930s. Ernst Ruska, a clever German engineer and one of the pioneer inventors of the transmission electron microscope (TEM), took note. In a speech at his Nobel prize award ceremony in 1986, Ruska famously said the following,

"The resolution limit of the light microscope due to the length of the light wave, which had been recognized 50 years before by Ernst Abbe and others, could, because of the lack of light, not be important at such magnifications. Knoll and I simply hoped for extremely low dimensions of the electrons. As engineers, we did not know yet the thesis of the "material wave" of the French physicist de Broglie that had been put forward several years earlier (1925). Even physicists only reluctantly accepted this new thesis. When I first heard of it in the summer of 1931, I was very much disappointed that now even at the electron microscope the resolution should be limited again by a wavelength (of the "Materiestrahlung"). I was immediately heartened, though, when with the aid of the de Broglie equation I became satisfied that these waves must be around five orders of magnitude shorter in length than light waves. Thus, there was no reason to abandon the aim of electron microscopy surpassing the resolution of light microscopy."

As de Broglie noted from Einstein's theory of special relativity, the calculation of a fast electron's wavelength (λ) having energies greater than 50keV must involve a relativistic correction as follows,

$$\lambda = \frac{h}{\left[2m_0eV\left(1+\frac{eV}{2m_0c^2}\right)\right]^{1/2}} \qquad 10.1$$

Indeed, the short wavelength of fast electrons, on the order of a couple of picometers, provides the resolution to observe atoms. Table 1 lists the electron wavelengths and velocities for different operating voltages in scanning and transmission electron microscopes.

Table 10.1 Calculation of electron wavelengths for different electron energies

Electron charge (e)	-1.602×10^{-19} C
1 eV	1.602×10^{-19} J
Electron rest mass (m_o)	9.109×10^{-31} kg
Electron rest energy (m_oc^2)	511 keV
Kinetic energy (charge x tension)	1.602×10^{-19} Nm (per 1 volt)
Plank's constant (h)	6.626×10^{-34} N-m-s
1 Ampere	1 C/sec
Light speed in vacuum (c)	2.998×10^{8} m/sec

non relativistic (<50keV)

$$\lambda = \frac{h}{(2m_0eV)^{1/2}}$$

Relativistic correction

$$\lambda = \frac{h}{\left[2m_0eV\left(1+\frac{eV}{2m_0c^2}\right)\right]^{1/2}}$$

Accelerating voltage [KV]	Nonrelativistic λ [nm]	Relativistic λ [nm]	Mass [x m_o]	Velocity [x 10^8 m/s]
1	0.03879	0.03878	1.002	0.13
10	0.01227	0.01221	1.02	0.42
80	0.00434	0.00418	1.157	1.1
200	0.00274	0.00251	1.391	1.59
300	0.00224	0.00197	1.587	1.82
1000	0.00123	0.00087	2.957	2.44

10.1.2 Spatial Resolution of TEMs

Spatial resolution is typically defined as the ability to distinguish between two closely spaced points, such as resolving an array of diffraction disks, and is referred to as diffraction-limited resolution. For

conventional light microscopes, the resolution is fundamentally limited by the wavelength of visible light. The Raleigh criterion can be used to define the diffraction-limited resolution,

$$d = 0.61\frac{\lambda}{n\sin\theta} = 0.61\frac{\lambda}{\beta} \quad 10.2$$

where n is the refractive index, λ is the wavelength, and β is the collection angle (inversely related to the numerical aperture), indicating that short wavelengths and high collection angles are essential for better resolution. As such, the resolution of visible-light optical microscopes was capped at approximately 200 nanometers (nm), limiting the ability to observe structures smaller than this threshold.

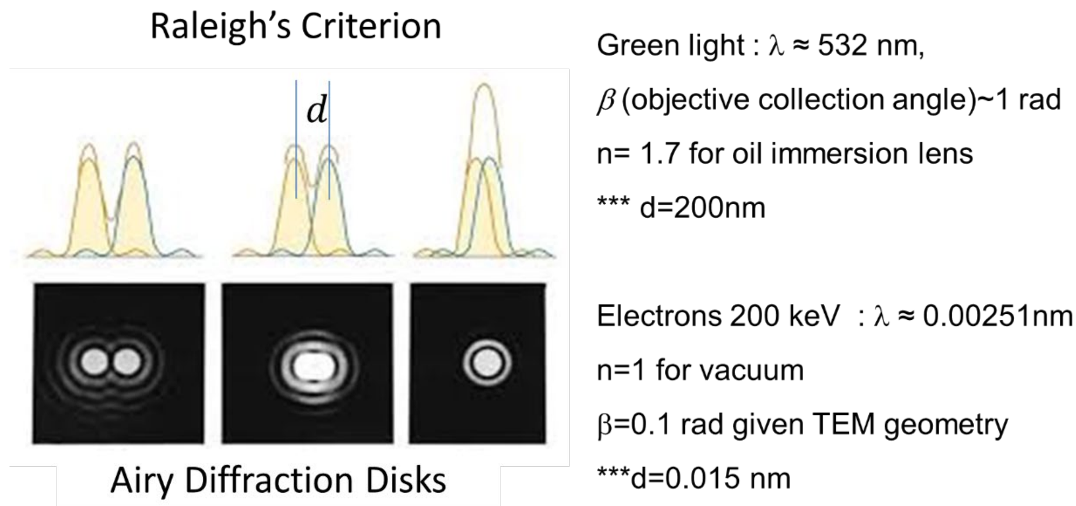

Figure 10.1 Schematic of the Raleigh criterion and comparison between optical and electron microscope resolution

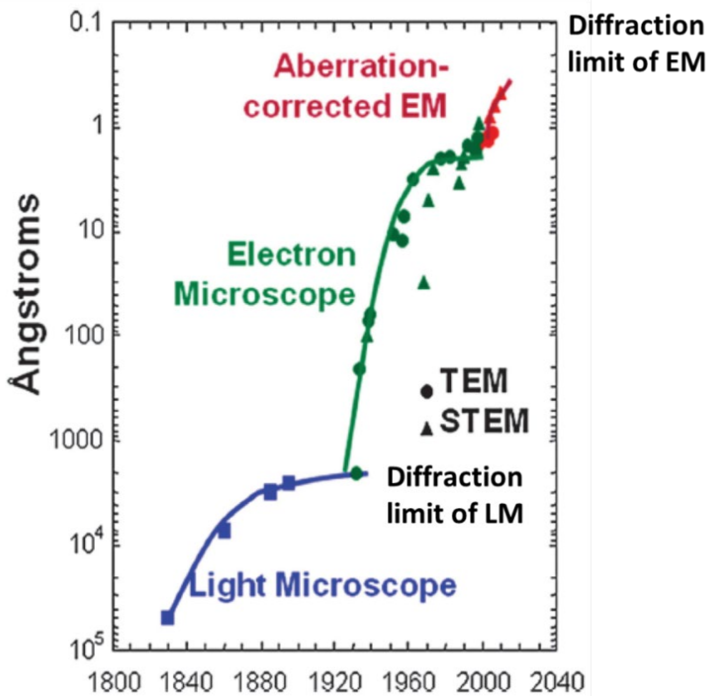

Figure 10-2: Plot of the evolution in microscope spatial resolution over 200 yrs.

It took decades of technological development to improve the quality of magnetic lenses and TEM electronics to a sufficient level to achieve atomic resolution. Yet, even in modern TEMs, the imperfections of the magnetic lenses (e.g., their spherical and chromatic aberrations) limit the achievable resolution to a factor of 100 above the diffraction limit (15 pm, as shown in Figure 10-1). The invention of aberration correctors and monochromators (improved electron sources) significantly improved resolution, providing picometer precision for determining sample structure (Figure 10-2). The widespread adoption of aberration correction in commercial TEMs has dramatically impacted the field of nanotechnology, enabling us to characterize atomic-scale defects and impurities in nanomaterials, which are

crucial for advancing their processing technologies and implementation in devices. Likewise, these technological improvements and new sensitive detectors in cryo-electron microscopy have enabled the solution of complex protein structures that cannot be crystallized and studied by standard Synchrotron X-ray scattering techniques. Electron microscopy has become an essential characterization tool for research in all physical sciences disciplines.

10.1.3 TEM construction

The Transmission Electron Microscope consists of 5 essential parts: (1) Electron gun, (2) Condenser lens, (3) Objective Lens, (4) Intermediate lenses, and (5) Detectors (See Figure 10-3).

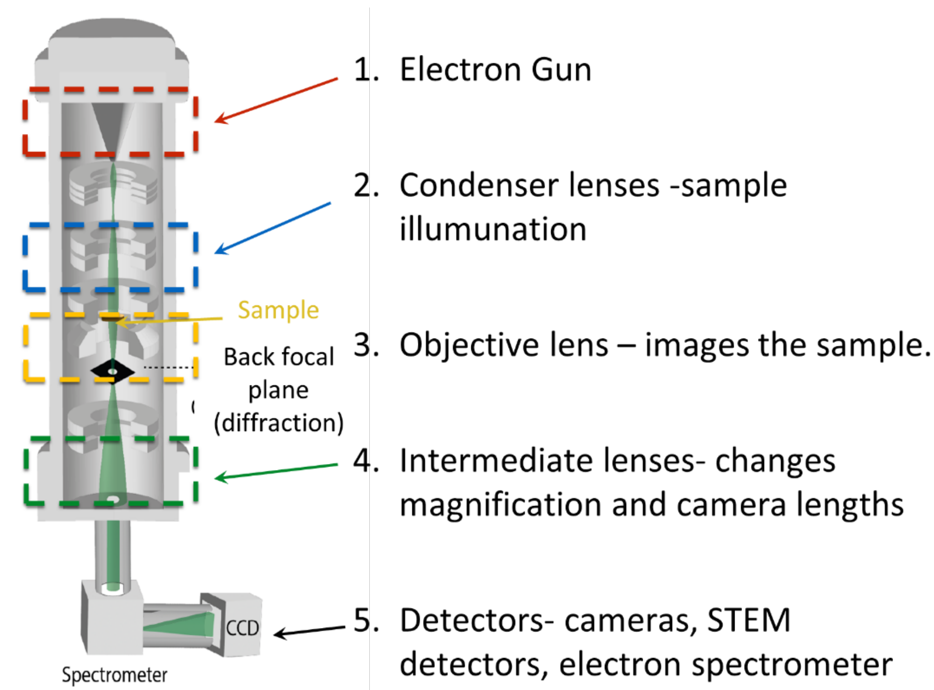

Figure 10-3: Basic Schematic TEM

The electron gun comprises the electron source, which can be a field emission or thermionic source, and the linear accelerator section consisting of a sequence of anode plates that can typically accelerate the electrons in the range of 30-300keV. Cold-field emission guns (CFEGs) use a sharp tungsten tip cooled to enhance electron emission with minimal thermal spread, providing high brightness and spatial coherence, ideal for high-resolution imaging. Schottky field emission guns (S-FEGs) combine thermally assisted field emission with a ZrO_2-coated tungsten tip, offering stability, longer lifetime, and high brightness, though with a slightly broader energy spread than C-FEGs. Both are suited for high-resolution applications, but S-FEGs are often preferred for their practical stability in routine operations.

Conversely, **thermionic guns** emit electrons via thermal excitation and exhibit lower spatial coherence and a higher energy spread than FEG guns. In TEM, thermionic guns typically have brightness values around 10^5 – 10^6 A/cm²·sr, considerably lower than field emission guns (FEGs), which can reach brightness levels above 10^8 - 10^9 A/cm²·sr. However, thermionic guns offer advantages over FEGs, including a more straightforward design, greater stability over time, longer operational lifetimes, and lower maintenance requirements, making them more cost-effective and robust for routine imaging applications where ultra-high resolution is not essential.

The condenser lens system controls the intensity and convergence of the electron beam on the sample. It typically consists of multiple electromagnetic lenses that shape and focus the beam emitted by an electron source, such as a thermionic or field-emission gun. By adjusting the condenser lenses, users can change the beam's brightness and spot size, allowing for fine-tuning of the electron dose on the sample. This control is crucial in TEM, as it affects the resolution, contrast, and amount of detail visible in the final image, e.g., for dislocation imaging. In addition, the condenser lenses enable switching between illumination modes, such as parallel illumination for high-resolution imaging and convergent-beam illumination for analytical techniques, such as electron diffraction.

The objective lens forms the specimen's magnified image and its corresponding diffraction pattern. It focuses the electron beam after interaction with the specimen, directing both transmitted and scattered electrons to converge at specific planes within the optical system: the image plane for real-space imaging and the back focal plane where the diffraction pattern forms, providing information on the sample's crystal structure and orientation., the sample is positioned in the object or eucentric plane of the objective lens, the plane where the sample can be tilted about its center without shifting the image or diffraction pattern, to reduce aberrations and obtain high spatial resolution. Proper alignment of the sample at the eucentric height allows for consistent focusing and easier analysis, especially when working with tilted samples in high-resolution or diffraction studies.

The intermediate and projection lens sections are crucial for forming and magnifying the electron image. The intermediate lens system adjusted the image magnification and the camera length of the diffraction pattern. The projection lens then further magnifies the image on a fluorescent screen or camera. TEMs often incorporate three intermediate lenses, which correct for image rotation caused by changes in the electrons' spiral trajectory within the focusing magnetic fields of the lenses, which can occur with varying magnifications or imaging settings. Knowing the image rotation between real-space and reciprocal space lattice vectors (diffraction imaging conditions associated with the $\vec{g}$) is essential for determining the dislocation image contrast, the Burgers vector ($\vec{b}$) using the invisibility criterion discussed in section §10.2.

Modern TEMs have many detectors that provide comprehensive information about a sample's structure, composition, and electronic properties (discussed in the next section), such as,

STEM Detectors (Brightfield, Darkfield, and HAADF): In scanning transmission electron microscopy (STEM) mode, detectors like brightfield, darkfield, and high-angle annular darkfield (HAADF) are used to capture images based on how electrons interact with the sample. Brightfield detectors utilize unscattered electrons to highlight dense areas as darker regions, while darkfield detectors use scattered electrons to observe specific structural details. HAADF detectors, capturing electrons scattered at high angles, provide high-contrast images sensitive to atomic number, making them ideal for atomic-resolution imaging and compositional mapping.

Electron Energy Loss Spectroscopy (EELS) Detectors: EELS detectors measure the energy loss of electrons as they pass through the sample, providing detailed information about the electronic structure and bonding. This technique is particularly valuable for analyzing light elements and subtle structural changes within the sample.

Charge-Coupled Device (CCD) Detectors: CCD detectors are commonly used in TEMs for direct digital imaging, converting electron interactions with the sample into electronic signals. Known for their high sensitivity and broad dynamic range, CCDs are ideal for capturing high-quality, high-resolution images, especially at low electron doses.

Complementary Metal-Oxide-Semiconductor (CMOS) Detectors: CMOS detectors, an alternative to CCDs, are known for their faster readout speeds and lower power consumption. Often used in applications requiring rapid image acquisition, CMOS detectors are robust and increasingly common in modern TEMs for high-resolution imaging with real-time analysis capabilities.

10.1.3 Interactions of fast electrons with TEM samples

Fast electrons are not only useful for probing the atomic structure of samples; they can be used to characterize a material's chemistry and electronic structure on the atomic scale. The interaction of high-energy electrons with matter involves complex scattering processes. It produces a variety of scattered electron signals and secondary particles, including plasmons, phonons, X-rays, and visible light. Figure 10-4 illustrates some of the scattered and secondary electrons produced in the TEM.

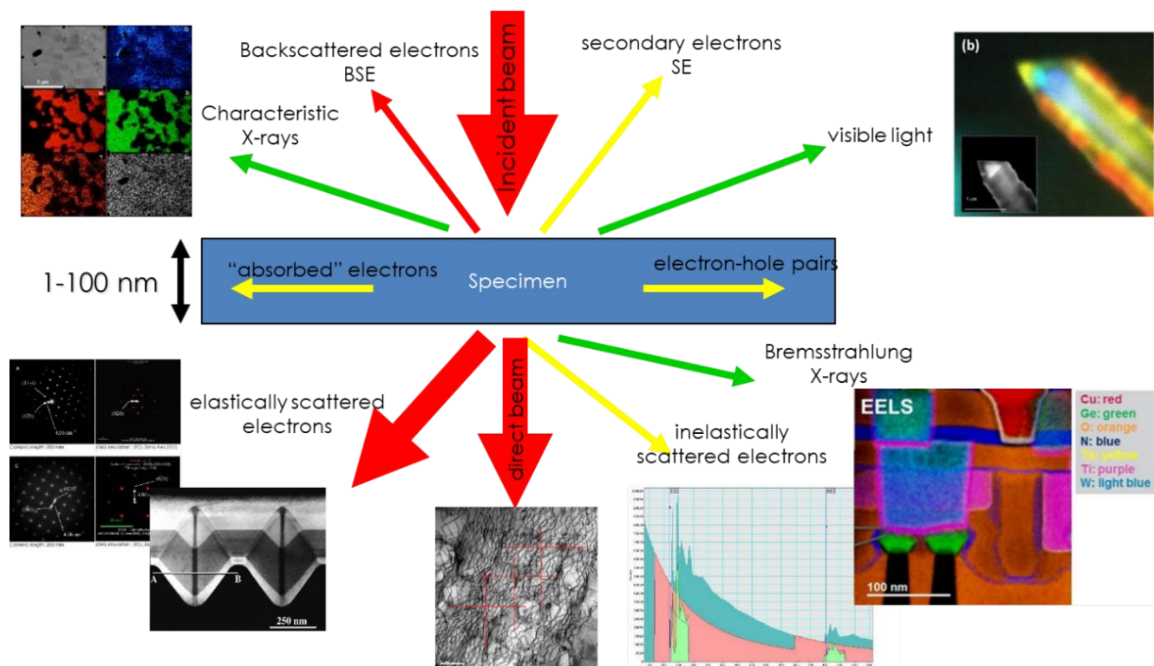

Figure 10-4: Schematic showing the imaging modes and sample characterization using the primary and secondary scattered signals produced by high-energy electron interactions with a thin TEM sample.

Typical TEM samples are sufficiently thin for electron transparency, on the order of 10-100nm. The interactions of fast electrons with materials can be subdivided into elastic and inelastic scattering. Elastic scattering can be described as electrons that do not transfer energy (elastic), while inelastic electrons lose significant energy due to scattering processes in the sample. We can also refer to the scattering process as coherent if the phase of the scattered electron waves is in phase. In contrast, incoherently scattered electrons have no phase relation among them. Here, we use the definitions of coherence and energy transfer (elastic and inelastic scattering processes) to describe different TEM modes and how these scattered signals can be used to characterize materials. This chapter focuses on diffraction and diffraction contrast imaging in TEM and STEM modes.

10.1.4 Diffraction and Imaging Modes

Since their invention, TEMs have been designed to operate in two distinct modes: imaging and diffraction. Bragg diffraction is a coherent, elastic scattering process in which the electron waves scattered from a periodic lattice constructively and destructively interfere (phase coherence). The

resulting patterns of coherently scattered electrons have intensities that quantitatively define the sample's atomic structure. The reciprocal lattice resolution of diffraction patterns is a measure of the transverse coherence of the electron beam; e.g., a typical modern 200kV TEM can have a transverse coherence length of a few μm.

With such resolution, electron diffraction can probe, for example, phase changes, crystallinity, crystal orientation, local charge states (e.g., charge density waves), phonon resonances, and magnetic ordering, amongst other periodic ordered structural characteristics of the sample. Figures 10-5a and 10-5b compare the difference between diffraction from a single crystal and a random polycrystal. The spot pattern of Figure 10-4a corresponds to the unit cell structure and orientation relative to the electron beam, the so-called zone axis, while the ring pattern of the polycrystal results from small crystals with random orientations, similar to patterns in X-ray diffraction Debye camera geometries. However, the diffracted electron intensities are challenging to interpret and require simulations (using Bloch wave theory) to determine quantitatively and account for dynamical elastic scattering effects.

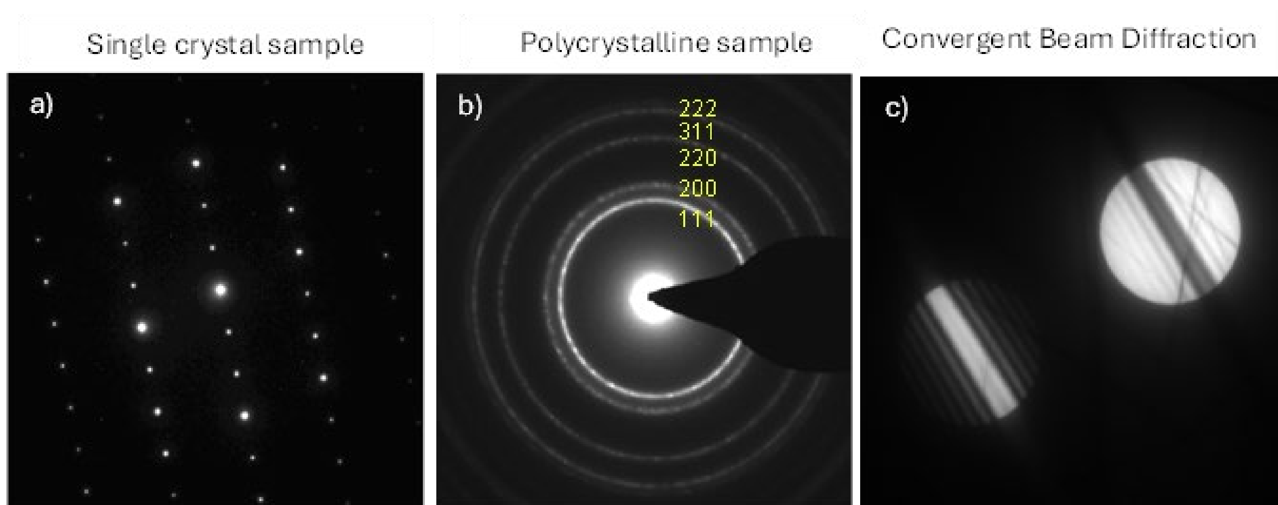

Figure 10-5: Typical diffraction patterns of TEM samples. a) A spot pattern formed single crystal in which pattern and its intensity relate to orientation and unit cell of the crystal, b) Debye ring patterns are generated for randomly oriented polycrystals, c) convergent beam electron diffraction (CBED) patterns exhibit multiple (dynamical) elastic scattering and coherent inelastic scattering of crystal atomic planes (excess and deficient lines) of the sample.

Since making TEM samples a few nanometers thick is challenging, most samples exceed the elastic-scattering mean free path, leading to multiple scattering. The repeated diffraction of electron waves by atomic periodicity produces constructive and destructive interference that depends on the sample lattice and thickness, resulting in a resonant intensity profile with sample thickness. For example, in the convergent beam diffraction pattern of Figure 5c, there is a thick dark line (called a deficient line) in the bright disk and a thick white line (excess) in the dark disk surrounded by multiple lines, which diminish in intensity. The diameter of the disks corresponds to the convergence angle, and the spacing between them is associated with the Bragg angle. The intensity in the disk consists of both incoherent scattering from all orientations and the excess and deficient lines resulting from coherent inelastic scattering from crystallographic planes (hkl). The intensity profile of the spots depends on the diffraction condition relative to the Ewald's sphere (see Figure 10-5a).

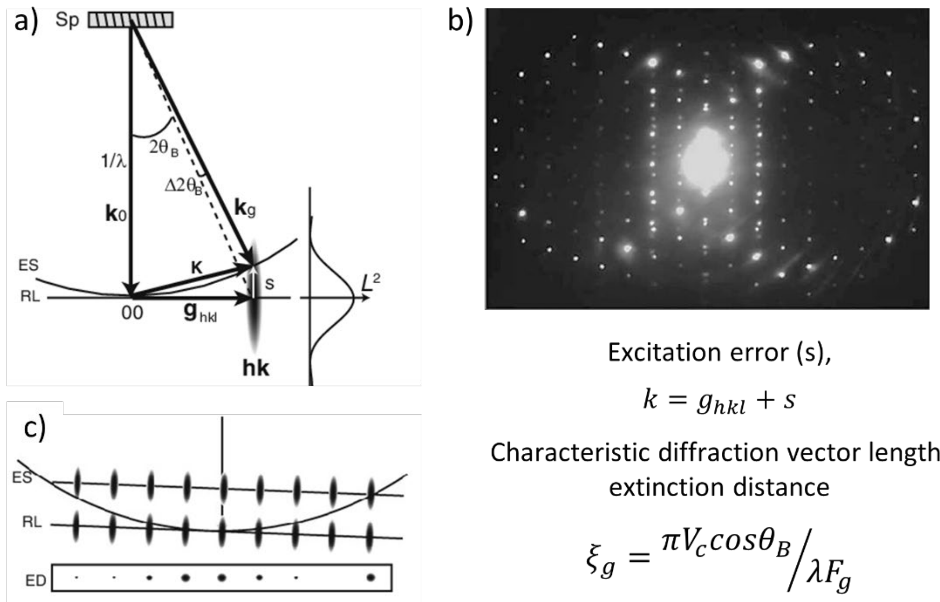

Figure 10-6: a) Schematic explaining the Ewald sphere construction in transmission electron diffraction and excitation error, b) Diffraction pattern showing rings of bright diffraction spots where the Ewald sphere intercepts the reciprocal lattice, c) 2-D schematic showing how the Ewald Sphere cuts through the relrods (reciprocal lattice rods of intensity).

The Ewald sphere (ES) is a geometrical construction used to determine which lattice planes satisfy the Bragg condition for diffraction. The radius of the Ewald sphere is inversely proportional to the electron wavelength, i.e., increases with increasing electron energy, and is centered at the origin of the reciprocal lattice ((000) diffraction spot). A lattice reflection, $\vec{g}$, intersects the sphere if the Bragg condition is met, resulting in diffracted beams and spots. However, due to the high energy of electrons (and hence their short wavelength) in TEM, the Ewald sphere is nearly flat, as seen in Figure 6, enabling diffraction from multiple crystallographic planes simultaneously.

The excitation error (s) quantifies the deviation of a reciprocal lattice point from the exact Ewald sphere surface and is given by:

$$s = \vec{k} - \overrightarrow{g_{hkl}} \qquad 10.3$$

where $\vec{k}$ is the wave vector of the incident beam. If $s = 0$, the lattice plane satisfies the Bragg condition exactly; if $s \neq 0$, the plane is slightly off-Bragg condition, resulting in reduced diffracted intensity. Figure 10-6 c illustrates the concept that $\boldsymbol{s}$ corresponds to Ewald sphere cutting through the ellipsoidal intensity distribution diffraction reflections ($\vec{g}$) and produce intensity variations in diffraction spots.

The extinction distance (ξ_g) represents the characteristic distance over which the electron beam exchanges intensity between the transmitted and diffracted beams due to multiple scattering in the crystal. It is a measure of the interaction strength between the electron wave and the crystal lattice planes and is given by:

$$\xi_g = \pi V_c cos\theta_B \Big/ \lambda F_g \qquad 10.4$$

where V_c is the unit cell volume, θ_B is the Bragg angle, λ is the electron wavelength, and F_g is the structure factor. When the crystal thickness approaches or exceeds the extinction distance, dynamical effects become significant, leading to complex intensity distributions in the diffraction pattern. The extinction distance also influences the spread of diffraction spots in reciprocal space and affects the

observed diffraction contrast, particularly in thicker crystals. This interplay is critical for understanding diffraction in both the kinematical and dynamical regimes, as well as for interpreting dislocation image contrast and character.

The diffraction patterns are generated in the back focal plane of the objective lens that forms the sample's high-resolution image (Figure 10-3). Changing the lens currents of the intermediate post-objective lens system changes the magnification and diffraction camera length. Inserting an aperture in the back focal plane to select and omit different diffracted beams allows the formation of an image exhibiting diffraction contrast and structural information about the sample, a technique commonly referred to as diffraction contrast imaging and yielding **Brightfield** and **Darkfield** images. Figure 10-7 shows an example of brightfield and darkfield imaging. This imaging technique is typically described as semi-coherent. Brightfield images hold information about morphology, grain size, and defect structures, while darkfield imaging can be used to correlate crystalline phase, orientation, and defect structures to grain morphologies and their distributions within the microstructure. Such techniques are powerful tools for characterizing phase transitions, defects, and their dynamics, as described later.

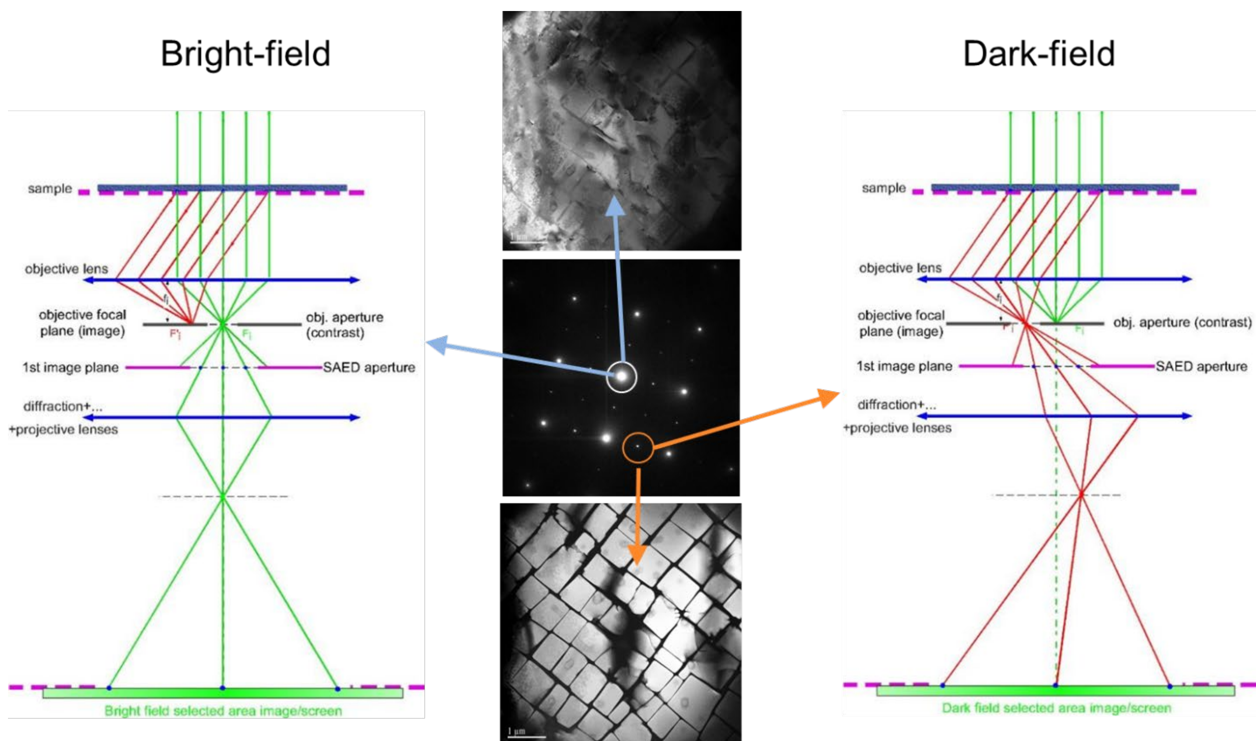

Figure 10-7: Diffraction contrast imaging using an objective aperture located in the back focal plane to form images from different scattering electron beams from the sample.

10.2 Howie Whelan Equations

The Howie-Whelan equations are fundamental for understanding electron diffraction contrast in TEM, particularly for defects such as dislocations. They describe the interaction between an electron wave and a crystalline material using a two-beam approximation. The equations are derived from the Schrödinger equation, which governs the propagation of electrons as wave functions through a periodic potential.

10.2.1 Kinematical and Dynamical Diffraction

Kinematical Diffraction Contrast theory assumes that only two beams—one direct and one diffracted—are considered, forming the basis for the two-beam condition. Figure 8 shows diffraction two-beam conditions in which various. $\vec{g}$ diffraction spots are excited in strong diffraction conditions.

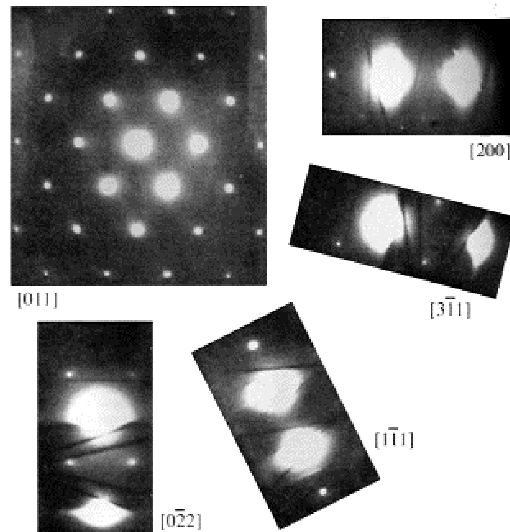

Figure 10-8: Different two-Beam conditions produced by tilting the sample away from [011] zone axis, the bracketed Miller indices represent different $\vec{g}$ vectors, which are used for dislocation analysis.

This model assumes single scattering, meaning only one scattering cycle influences the intensity, with minimal absorption, so that $I_{trans} = 1 - I_{diff}$. The intensity of the diffracted beam, I_{diff}, can be described by the equation:

$$I_{diff} = \frac{sin^2(\pi zs)}{\xi_g s^2} \tag{10.5}$$

where z is the thickness of the crystal, s is the excitation error, and $\xi_g$is the extinction distance given by equation 10-8.

In Dynamical Diffraction Contrast conditions, multiple scattering events are frequent, as electrons undergo repeated diffraction interactions between lattice planes, and contribute significantly to the modulation of observed contrast, making this model suitable for thicker samples. Unlike the simple single scattering in the kinematical model, dynamical diffraction involves more complex interactions, where the electron waves diffract multiple times, resulting in enhanced contrast and more intricate interference patterns. Dynamical scattering contrast around defects, combined with its nanometer-scale image resolution, has made Transmission Electron Microscopy a unique and invaluable tool for characterizing dislocations.

Thickness fringes are a specific manifestation of dynamical diffraction contrast, arising from variations in crystal thickness in regions of strong diffraction. Thickness fringes occur due to interference between the transmitted and diffracted beams, with the crystal thickness and excitation conditions modulating the phase relationship. For example, in the wedge-shaped sample shown in Figure 10-9, dark fringes appear with multiples of 0.5 of the extinction distance, ξ_g . These thickness fringes are particularly pronounced in areas with structural irregularities, such as stacking faults, dislocations, grain boundaries, and phase boundaries, where localized changes in the amplitude and phase of the electron wave occur.

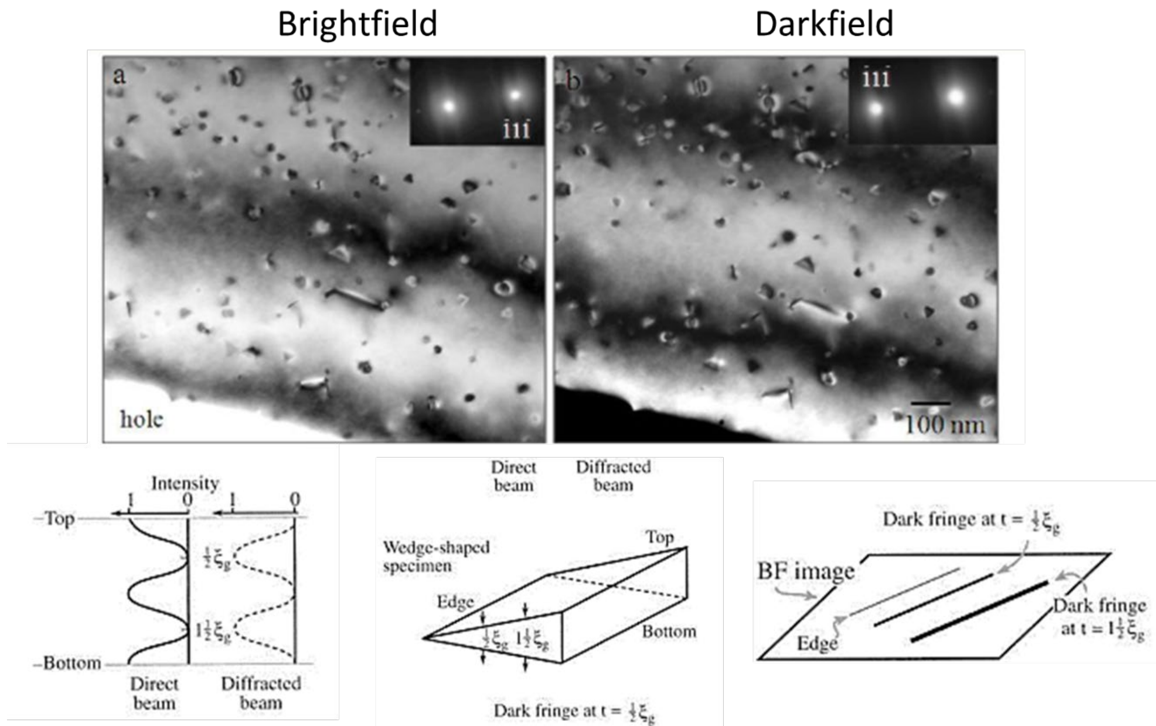

Figure 10-9: Example of thickness fringes that arise from the constructive and destructive interference from dynamical or multiple scattering events in which dark and bright fringes appear at multiples of the extinction distance in a wedge-shaped TEM sample. The speckle-like contrast arises from the strain fields of small dislocation loops.

These multiple "dynamical" scattering effects due to thickness variations are influenced by the crystal's internal strain and lattice distortions, and the contrast and fringes appearing around defects, due to their localized strain fields, can be used to visualize their detailed structures, e.g., size, crystallography, and a dislocation's Burgers vector.

Diffraction contrast is highly sensitive to crystal imperfections, such as stacking faults, grain boundaries, translation boundaries, phase boundaries, and stepped surfaces. These defects introduce localized distortions in the crystal lattice, leading to variations in the amplitude and phase of the electron wave as it passes through the material. The resulting interference patterns, arising from constructive and destructive interference, produce fringe patterns in the diffraction contrast image that reveal detailed information about the nature and distribution of these defects.

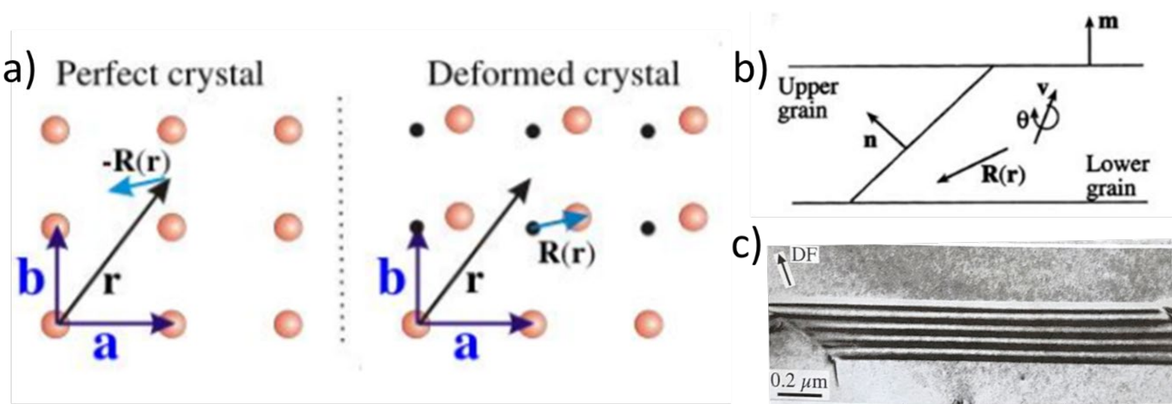

Figure 10-10: a) and b) schematic showing the lattice distortion and translation vector leading to a change in the local potential and to dynamical scattering effects, such as the fringes in d) a darkfield TEM image of a stacking fault image with two-beam condition.

For example, the potential of a perfect can be given by the following expression,

$$V(r) = \sum_g V_g e^{2\pi i \boldsymbol{g}\cdot r} \quad 10.6$$

where $\boldsymbol{g}$ is the reciprocal lattice vectors, and $\boldsymbol{g}\cdot r$ represents the periodicity of the crystal lattice. For a crystal with a defect, the potential $V_{def}(r)$ can be expressed as a sum over the reciprocal lattice vectors $\boldsymbol{g}$, incorporating a phase factor that reflects the defect's effect on the crystal structure:

$$V_{def}(r) = \sum_g V_g e^{2\pi i \boldsymbol{g}\cdot[\boldsymbol{r}-\boldsymbol{R}(\boldsymbol{r})]} \quad 10.7$$

where V_g is the amplitude of the potential associated with the lattice planes, and $\boldsymbol{r}-\boldsymbol{R}(\boldsymbol{r})$ denotes the position of the defect. This equation illustrates how translations and rotations between different crystal regions can cause periodic variations in the electron wave amplitude, resulting in the fringe patterns observed in brightfield and darkfield imaging modes. The appearance of the stacking fault in Figure 10-10 d) depends on the thickness and two-beam diffraction conditions. These patterns provide essential insights into the structural irregularities, enabling researchers to examine the nature of defects and the associated lattice distortions.

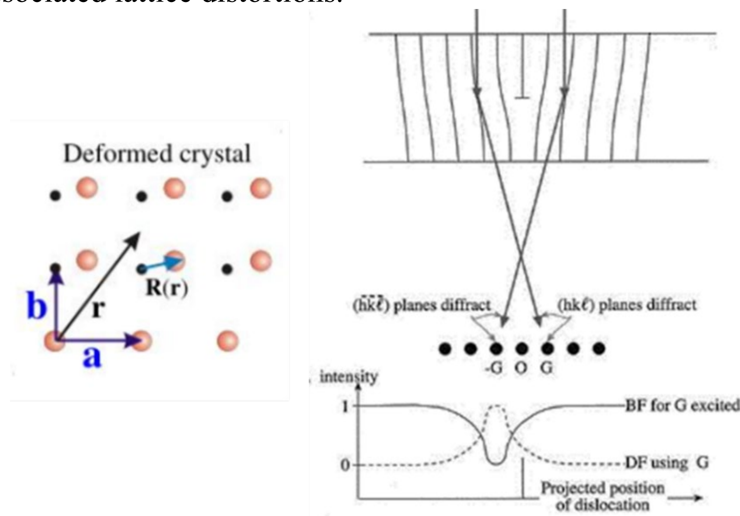

Figure 10-11 Schematic showing how the lattice distortion around a dislocation core leads to increased diffracted signals, R(r) in this case is the Burgers vector

10.2.2 Using the Howie-Whelan equations to interpret dynamical diffraction contrast around defects

For a crystal with a dislocation, the local lattice strain field alters the phase and amplitude of the transmitted and diffracted electron beams. In the two-beam case, where only the transmitted beam and one intense diffracted beam (generated due to Ewald's sphere cutting through the center of the diffracted beam relrod) are considered, the equations are,

$$d\phi_o = \left\{\frac{\pi i}{\xi_g}\phi_g e^{-2\pi i \boldsymbol{K}\cdot\boldsymbol{r}} + \frac{\pi i}{\xi_o}\phi_o\right\}dz \text{ and } d\phi_g = \left\{\frac{\pi i}{\xi_g}\boldsymbol{\phi_o} e^{2\pi i \boldsymbol{K}\cdot\boldsymbol{r}} + \frac{\pi i}{\xi_o}\phi_g\right\}dz \quad 10.8$$

where ϕ_o and ϕ_g are the amplitudes of the transmitted and diffracted beams, respectively, $\boldsymbol{z}$ is the direction of propagation of the electron beam through the crystal, ξ_g and ξ_o the extinction distances of the diffracted and transmitted beams given by equation 10.8, and $\boldsymbol{K}\cdot\boldsymbol{r}$ is the scattering of the electron wave in the periodic crystal.

The amplitudes of ϕ_g and ϕ_o are coupled and change with propagation in the sample. Solving these coupled differential equations gives the intensity distribution of the transmitted and diffracted beams. The interaction of these beams results in the characteristic diffraction contrast observed in TEM images.

$$\frac{d\phi_o}{dz} = \left\{\frac{\pi i}{\xi_g}\phi_{\boldsymbol{g}} e^{2\pi i s z} + \frac{\pi i}{\xi_o}\phi_o\right\} \text{ and } \frac{d\phi_g}{dz} = \left\{\frac{\pi i}{\xi_g}\phi_{\boldsymbol{o}} e^{-2\pi i s z} + \frac{\pi i}{\xi_o}\phi_g\right\}, sz = \boldsymbol{s}\cdot\boldsymbol{r} \qquad 10.9$$

where $\boldsymbol{s}$ is the excitation error, which quantifies the deviation from the exact Bragg condition, and when $sz = \boldsymbol{s}\cdot\boldsymbol{r} \neq \boldsymbol{0}$, there is diffraction contrast. The scattering amplitude of the diffraction contrast can be calculated by solving Schrödinger's equations.

$$\phi_g = \frac{\pi a i}{\xi_g} e^{2\pi i \boldsymbol{K}\cdot\boldsymbol{r_a}} e^{2\pi i \boldsymbol{k}_g\cdot\boldsymbol{r}} \qquad 10.10$$

The total wavefunction in the two-beam condition is given by,

$$\Psi_T = \phi_o e^{2\pi i \boldsymbol{k}_o\cdot\boldsymbol{r}} + \phi_{g1} e^{2\pi i \boldsymbol{k}_{g1}\cdot\boldsymbol{r}} + \phi_{g2} e^{2\pi i \boldsymbol{k}_{g2}\cdot\boldsymbol{r}} + \phi_{g3} e^{2\pi i \boldsymbol{k}_{g3}\cdot\boldsymbol{r}} \ldots \qquad 10.11$$

In the 2-beam condition, only the first two terms are considered. Note that $\boldsymbol{r}$ and $\boldsymbol{s}$ are parallel to $\boldsymbol{z}$. The scattering amplitudes can be put in terms of γ the phase of the electron beam.

$$\begin{aligned} \phi_o &= C_o e^{2\pi i \gamma z}, \\ \phi_g &= 2\xi_g \gamma C_o e^{2\pi i \gamma z} \end{aligned} \qquad 10.12$$

When a dislocation is present, the local strain field changes the values of s_R and $\phi_g(z)'$, leading to contrast variations that are crucial for determining the Burgers vector and line direction:
The amplitude of the transmitted beam propagating along z,

$$\phi_o(z)' = \phi_o \exp\left(\frac{-\pi i z}{\xi_o}\right) \qquad 10.13$$

The scattering amplitude of the diffracted beam is phase shifted by the lattice translation and distortions produced by a defect and is given as follows:

$$\phi_g(z)' = \phi_g \exp\left(2\pi i s z - \frac{\pi i z}{\xi_o} + 2\pi i \boldsymbol{g}\cdot\boldsymbol{R}(\boldsymbol{r})\right) \qquad 10.14$$

The interaction of these transmitted and diffracted beams in a two-beam condition produces a diffraction contrast around the defect described by the following relation,

$$d\phi_g = \left(\frac{\pi i}{\xi_g}\phi_o(z)' + 2\pi i s_R \phi_g(z)'\right) dz \text{ and } s_R = s + \boldsymbol{g}\cdot\frac{\boldsymbol{dR}(\boldsymbol{r})}{dz} \qquad 10.15$$

When $\boldsymbol{g}\cdot\boldsymbol{R}(\boldsymbol{r}) = \boldsymbol{0}$ there is no phase shift and amplitude contrast around the defect, i.e., it is invisible. Since $\boldsymbol{R}(\boldsymbol{r}) = \vec{\boldsymbol{b}}$ for dislocation, $\boldsymbol{g}\cdot\boldsymbol{b} = \boldsymbol{0}$ can be used as a criterion for determining the dislocation character. For stacking faults, the fringes appear with distinct patterns related to the crystallography of the stacking faults, e.g., intrinsic or extrinsic Frank a/3<111> type stacking fault. See Table 2 and Figure 10-12.

Table 2. Amplitude Contrast variation around different stacking faults under different two-beam imaging conditions

	$\boldsymbol{R}(\boldsymbol{r})$	$\boldsymbol{g}$	$\boldsymbol{2\pi g\cdot R}$
SF in FCC	$\frac{1}{3}[111]$	(111), (220),(113)	$2\pi/3$
SF in FCC	$\frac{1}{6}\,[11\bar{2}]$	(111) (220)	0 $4\pi/3$

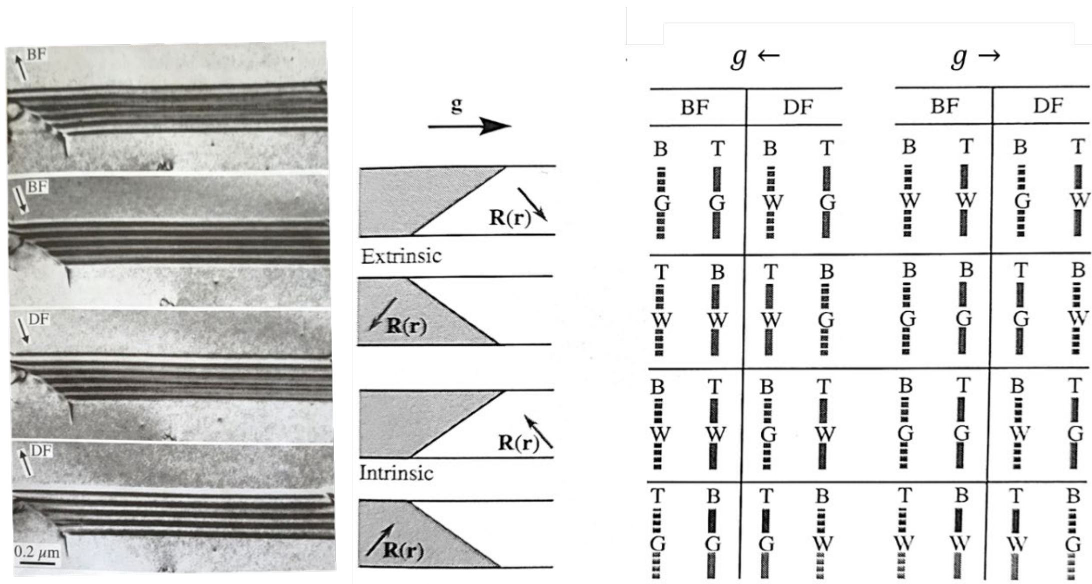

Figure 10-12: A series of brightfield and darkfield TEM images of a Frank stacking fault under different two-beam diffraction conditions. By observing the fringe contrast, the crystallographic properties of this stacking fault can be determined.

For screw dislocation, the invisible criterion follows the radial displacement field due to the Burgers vector being parallel to the dislocation line.

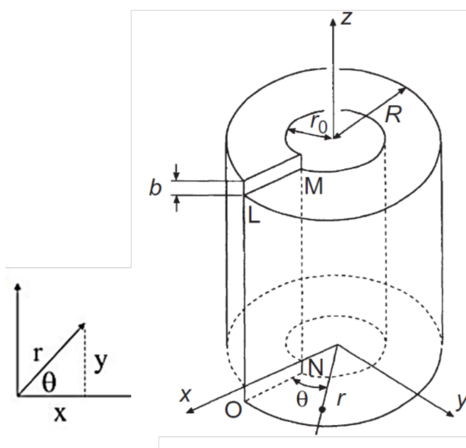

Shear Deformation along z directions on (r,z) plane

$$u_r = u_\theta = 0 \qquad u_z = \frac{b\theta}{2\pi} \tag{10.16}$$

$$R(x,y) = \frac{\boldsymbol{b}}{2\pi}tan^{-1}\left(\frac{x}{y}\right) \tag{10.17}$$

The contrast extinction condition require

$$\boldsymbol{g}\cdot\boldsymbol{R} = 0, \pm 1, \ldots \rightarrow \boldsymbol{g}\cdot\boldsymbol{b} = \boldsymbol{0} \tag{10.18}$$

Figure 10-13: Displacement field of a screw dislocation

Since the Burgers vector is perpendicular to the dislocation line, the invisible criterion for an edge dislocation is more involved and follows,

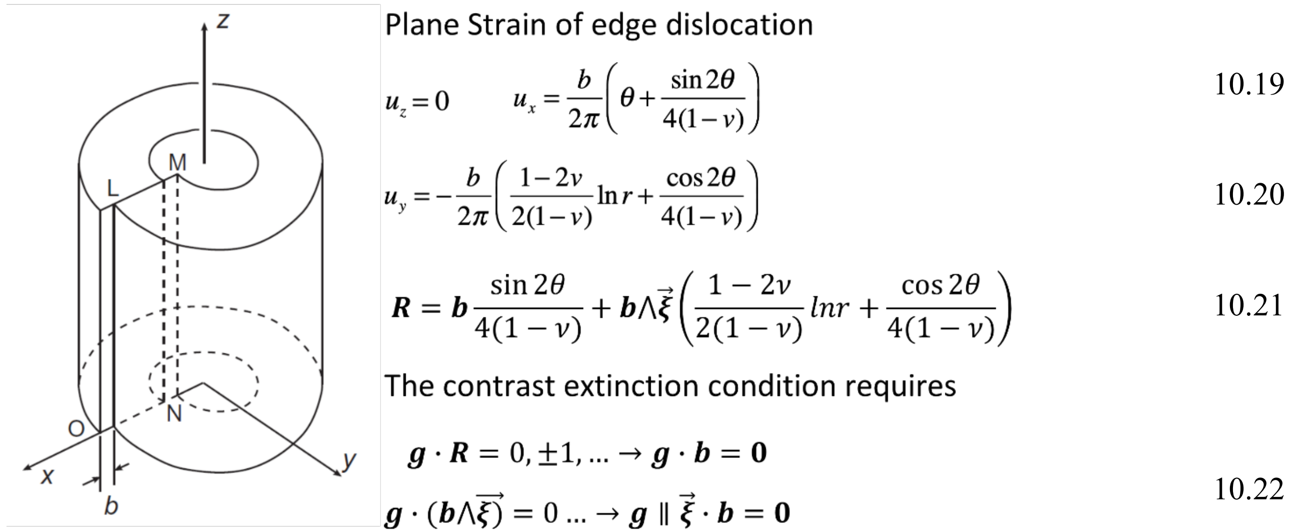

Figure 10-14: Displacement field of an edge dislocation

10.3 Characterization of Dislocations Using TEM Imaging Techniques

Three key imaging techniques are used to study dislocations in TEM: brightfield (BF), darkfield (DF), and weak-beam darkfield (WBDF). Each technique exploits the diffraction contrast governed by the Howie-Whelan equations to reveal different aspects of the dislocation structure.

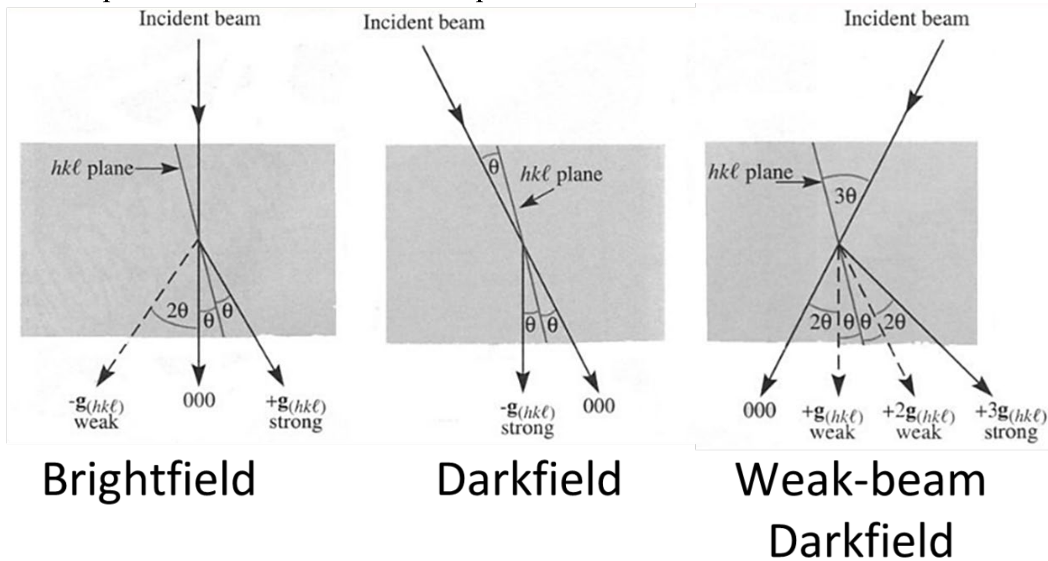

Figure 10-15: Ray diagrams for different imaging modes

10.3.1 Brightfield Imaging

Brightfield (BF) imaging is one of the most commonly used TEM techniques for dislocation analysis. In BF imaging, the central transmitted beam passes through the objective aperture, while any diffracted beams are excluded. The dislocation contrast in BF images is primarily determined by variations in the intensity of the transmitted beam resulting from changes in diffraction conditions around the dislocation core.

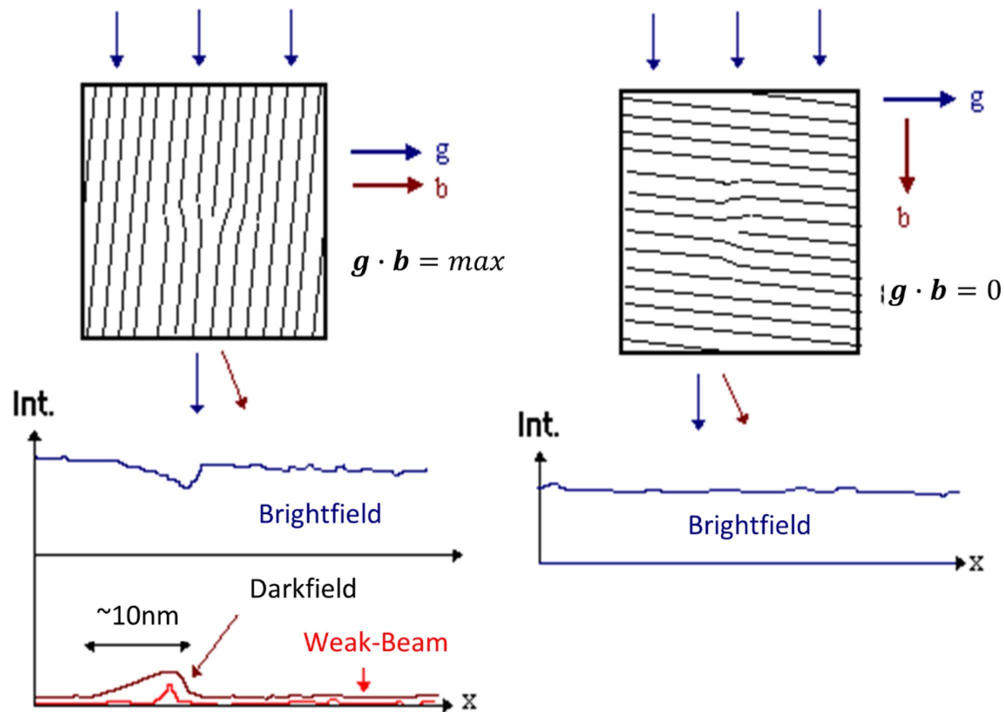

Figure 10-16: Schematic showing how imaging using different two-beam conditions with different $\vec{g}$ vectors: the visibility of a dislocation depends on its Burgers vector.

10.3.2 DarkField Imaging

Darkfield (DF) imaging is achieved by selecting a diffracted beam (rather than the transmitted beam) using the objective aperture. This technique provides higher contrast for specific features, such as dislocations and stacking faults, compared to brightfield imaging. In DF mode, the diffraction condition is critical in determining whether a dislocation is visible. That is, the "g·b" criterion applies to DF imaging as well, but in this mode, contrast is often more sensitive to the strain field of the dislocation. DF imaging is particularly useful for imaging edge and mixed dislocations, where strain fields can extend over large areas. Contrast in DF images is primarily influenced by variations in diffracted intensity resulting from changes in the local strain field near the dislocation. The contrast formation is similar to BF imaging, but since the diffracted beam is used, slight variations in diffraction conditions can produce significant changes in the image contrast.

10.3.3 Weak-Beam Darkfield Imaging

Weak-beam darkfield (WBDF) imaging is a more advanced technique that enhances the visibility of strain fields around dislocations while minimizing other contrast sources such as thickness fringes. In WBDF, the objective aperture is centered around a diffracted beam under a slightly off-Bragg condition. This condition ensures that only high-order interactions contribute to the image, making dislocation cores and fine details of the strain field more visible.

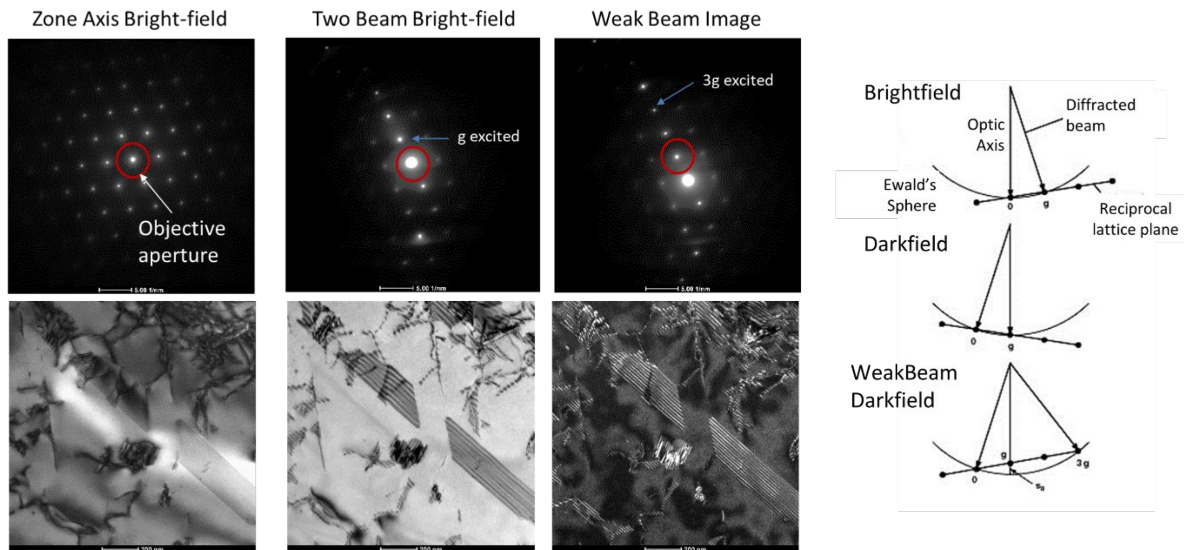

Figure 10-17: Series of imaging under different diffraction conditions comparing the width of the diffraction contrast around the dislocation and stacking in the FCC intermetallic CoCr alloy.

The contrast in WBDF images is highly sensitive to both $\boldsymbol{g}$ and $\boldsymbol{s}$, making it ideal for detailed characterization. Note that under the "kinematical" zone-axis and two-beam diffraction conditions, the contrast is strong and spatially broad, blurring details of the dislocation structures. The primary advantage of WBDF over BF and DF is its ability to provide high-resolution images of the dislocation core structure. The enhanced contrast enables more accurate determination of the Burgers vector and the dislocation line direction.

10.3.4 Determination of Burgers Vector and Line Direction

The precise determination of the Burgers vector and line direction is essential for understanding the type and behavior of dislocations in a material. The Burgers vector characterizes the magnitude and direction of lattice distortion caused by the dislocation. By using a combination of BF, DF, and WBDF techniques, it is possible to determine $\vec{\boldsymbol{b}}$ and the line direction $\vec{\xi}$ with high accuracy. The so-called "$\boldsymbol{g} \cdot \boldsymbol{b}$ criterion", where $\vec{\boldsymbol{g}}$ is the diffraction vector and $\boldsymbol{b}$ is the Burgers vector, is used to determine whether a dislocation will be visible:

- A dislocation will appear in BF imaging with maximum contrast if $\vec{g} \parallel \vec{b}$.
- When $\boldsymbol{g} \cdot \boldsymbol{b} = \boldsymbol{0}$, no contrast is observed.
- If it is an edge dislocation, no contrast must also be observed $\boldsymbol{g} \cdot \boldsymbol{b} \wedge \boldsymbol{\xi} = \boldsymbol{0}$

Using this criterion, BF imaging can be employed to identify the Burgers vector of a dislocation by selecting different diffraction conditions and examining which dislocations appear or disappear in the image. To apply this method:

- Select a series of diffraction conditions using different diffraction vectors $\vec{\boldsymbol{g}}$.
- Record images under each condition and note which dislocations are visible.
- Use the visibility rules: a dislocation will only appear if $\boldsymbol{g} \cdot \boldsymbol{b} = \boldsymbol{0}$, and find at least two $\boldsymbol{g_1}$ and $\boldsymbol{g_2}$ that meet this criterion.
- By systematically varying $\vec{\boldsymbol{g}}$ and observing contrast changes, the components of $\vec{\boldsymbol{b}}$ and the line direction $\vec{\xi}$ can be determined.

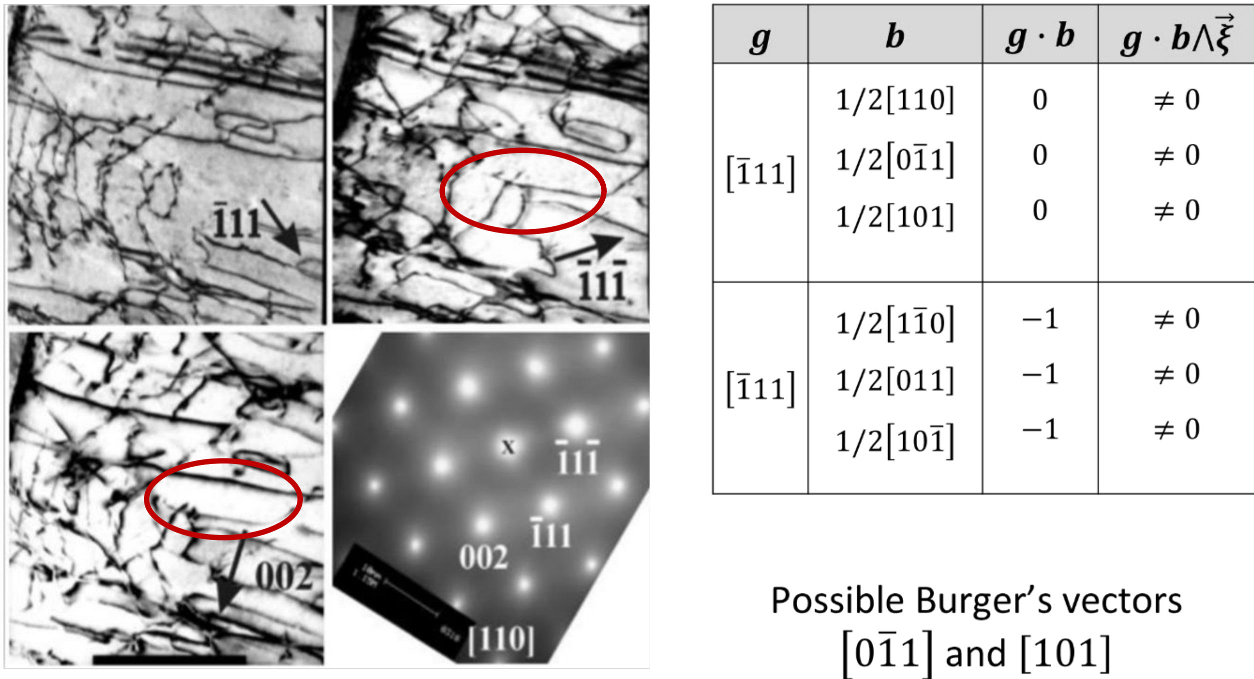

g	b	$g \cdot b$	$g \cdot b \wedge \vec{\xi}$
$[\bar{1}11]$	$1/2[110]$	0	$\neq 0$
	$1/2[0\bar{1}1]$	0	$\neq 0$
	$1/2[101]$	0	$\neq 0$
$[\bar{1}11]$	$1/2[1\bar{1}0]$	-1	$\neq 0$
	$1/2[011]$	-1	$\neq 0$
	$1/2[10\bar{1}]$	-1	$\neq 0$

Figure 10-18: An example dislocation analysis. The montage on the left shows a series of TEM brightfield images taken under different two-beam conditions and $\vec{g}$ vectors. The red ellipses mark dislocations invisible to $\vec{g}= [\bar{1}11]$ but visible with $\vec{g}= [\bar{1}1\bar{1}], [002]$. Using the table on the right, these dislocations must have Burgers vector of $[0\bar{1}1]$ or $[101]$.

10.4 Scanning TEM dislocation imaging

In STEM, a finely focused electron beam is rastered over the sample, enabling detailed analysis of local atomic structure, chemistry, and electronic structure, as discussed in section 10.2.3. STEM imaging modes, including high-angle annular darkfield (HAADF) and brightfield STEM, are particularly suited for imaging dislocations. Compared to conventional TEM imaging, diffraction-contrast imaging in scanning transmission electron microscopy, when appropriately configured, can provide better defect contrast with almost negligible bend-contour artifacts, enabling more effective analysis of dislocation structures. The main advantage of imaging dislocation in STEM mode is that it reduces the contrast of bend contours, which commonly obscure underlying defect structures. Under such diffraction contrast conditions, the electron microscope parameters for STEM imaging must strictly comply with the principle of reciprocity, such that the STEM probe convergence angle, α_S, is similar to the collection angle (the size of the objective aperture) for brightfield TEM imaging, β_T, on the order of 5 mrad. Having the STEM imaging mode convergence and collection semi-angles, α_S and β_S, a few milliradians in size, is essential for bend-contour-free defect imaging. These conditions can be appropriately set by adjusting the camera length and using the appropriate STEM detectors.

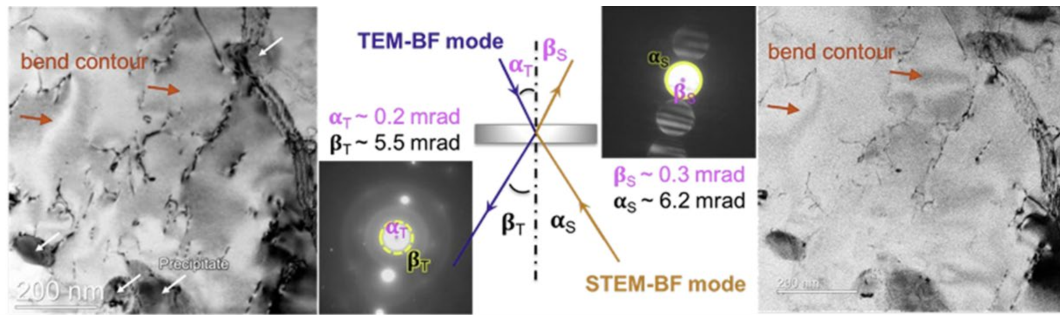

Bend Contour contrast is suppressed when $\beta_S \approx \alpha_S$

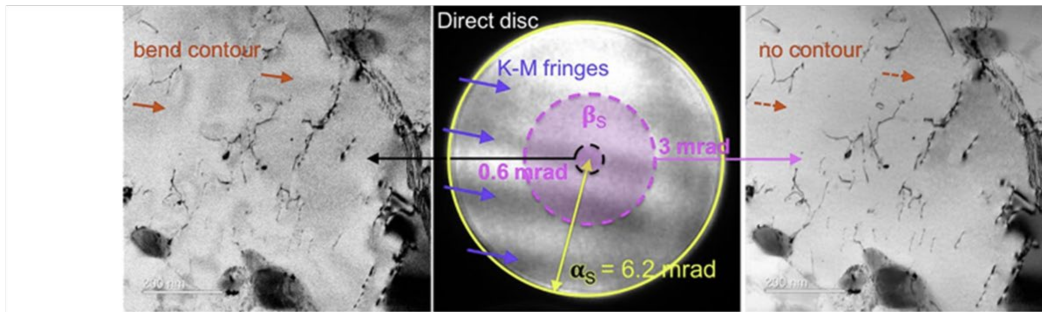

Figure 10-19: Upper montage of images shows that having a STEM probe convergence angle similar to the TEM brightfield collection angle provides good diffraction contrast. The lower series of images demonstrates that when the probe convergence and collection angles are similar and on the order of a few milliradians, bend contours are suppressed.

10.4.1 High-Angle Annular Darkfield (HAADF) Imaging:

HAADF is one of the most widely used STEM modes for dislocation analysis. In HAADF STEM, electrons scattered at high angles are collected, producing images where contrast is roughly proportional to the atomic number (Z-contrast). This technique provides atomic-resolution images in which heavier elements appear brighter, making it useful for heterogeneous materials.

Focused e⁻ probe scanned on sample; disc and annular detectors in back focal (diffraction) plane

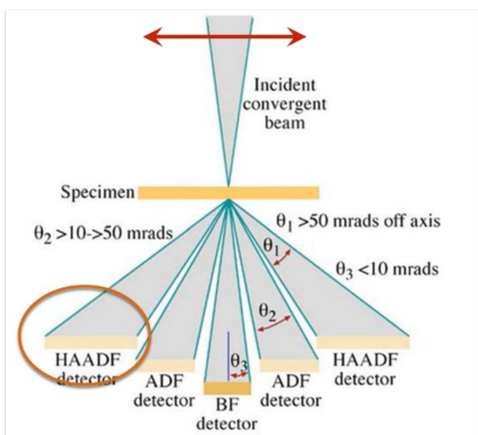

High-angle annular dark-field => compositional contrast: intensity ∝ $Z^2 t$ (thickness t, atomic number Z)

Z-contrast examples:

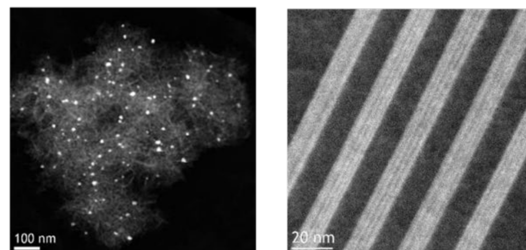

Pt catalyst on Al_2O_3 Si-Ge/Si multilayer

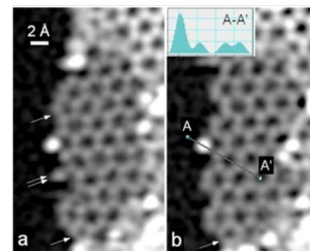

Cs-orcrected - graphene with dopant atoms (Krivanek et al., Nion)

Figure 10-20: The Left image is a schematic ray diagram of an HAADF STEM image. The series of HAADF STEM images on the right demonstrates image contrast arising from differences in the atomic number.

HAADF imaging can directly visualize the core structure of dislocations, including both edge and screw dislocations, by highlighting the distortions and extra half-planes of atoms around the dislocation line. Since HAADF imaging is sensitive to atomic structure and strain fields, it allows researchers to identify the Burgers vector. This key parameter describes the magnitude and direction of a dislocation. Moreover, the probe convergence and collection angles in aberration-corrected HAADF STEM imaging are similar and can suppress the bend contour contrast, as shown in Figure 10-21a). The"$\boldsymbol{g} \cdot \boldsymbol{b} = \mathbf{0}$ criterion" also applies to the HAADF image. By tilting to a specific zone axis, the atomic structure of the dislocation core can be observed with aberration-corrected high-resolution STEM, as shown in Figure 10-21d).

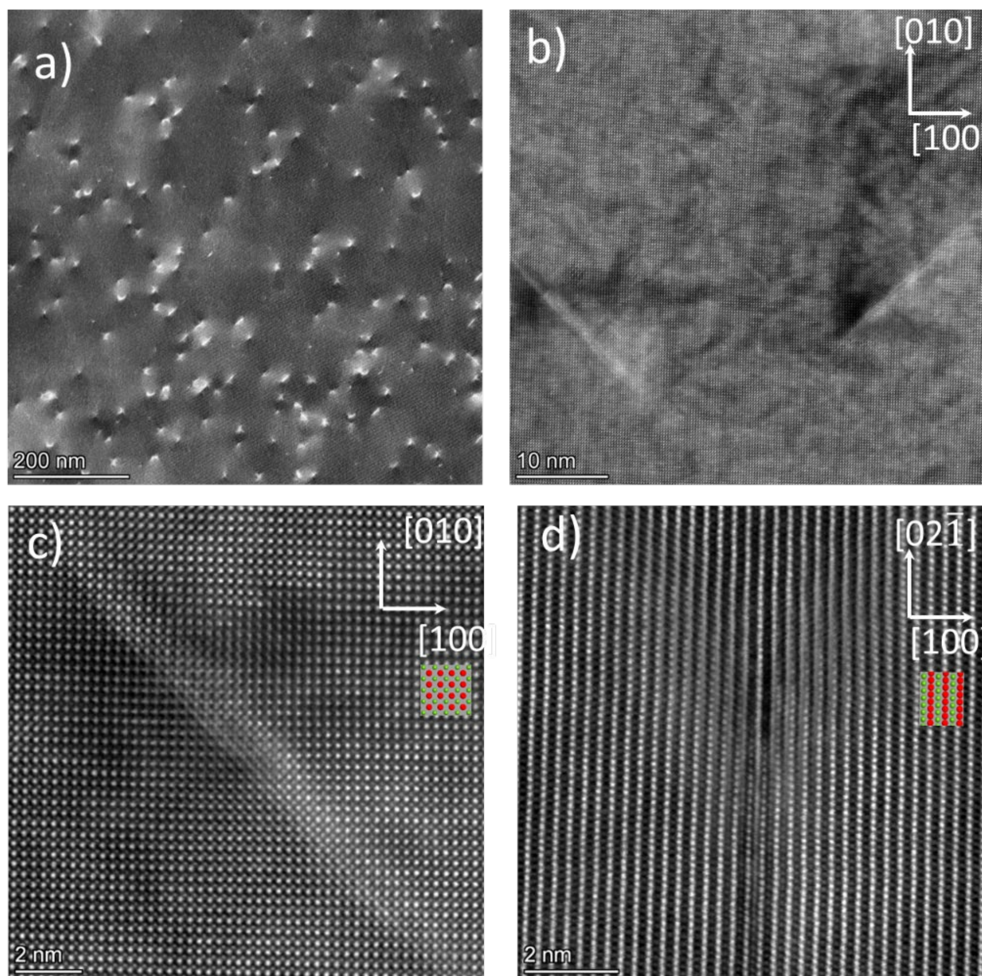

Figure 10-21: a) Low magnification HAADF STEM of misfit dislocations in epitaxial FeRh films grown on MgO substrates. Image acquired with $\beta_S(24mrad) \approx \alpha_S(20mrad)$. b) High magnficaiton HAADF image of pair of a<111> type screw dislocation lying on inclined {110} planes of B2 (BCC) FeRh. c) Atomically resolved image of a screw misfit dislocation. d) atomically resolved image of a[100] type misfit edge dislocation in the FeRh film.

10.4.2 Fourier Filtering

Fourier filtering can help visualize the dislocation character and core structure. A fast Fourier transform (FFT) of the image is performed, and spatial frequencies related to the lattice distortions are selected and masked. The inverse Fourier transform is taken of the masked FFT, as shown in Figure 10-22.

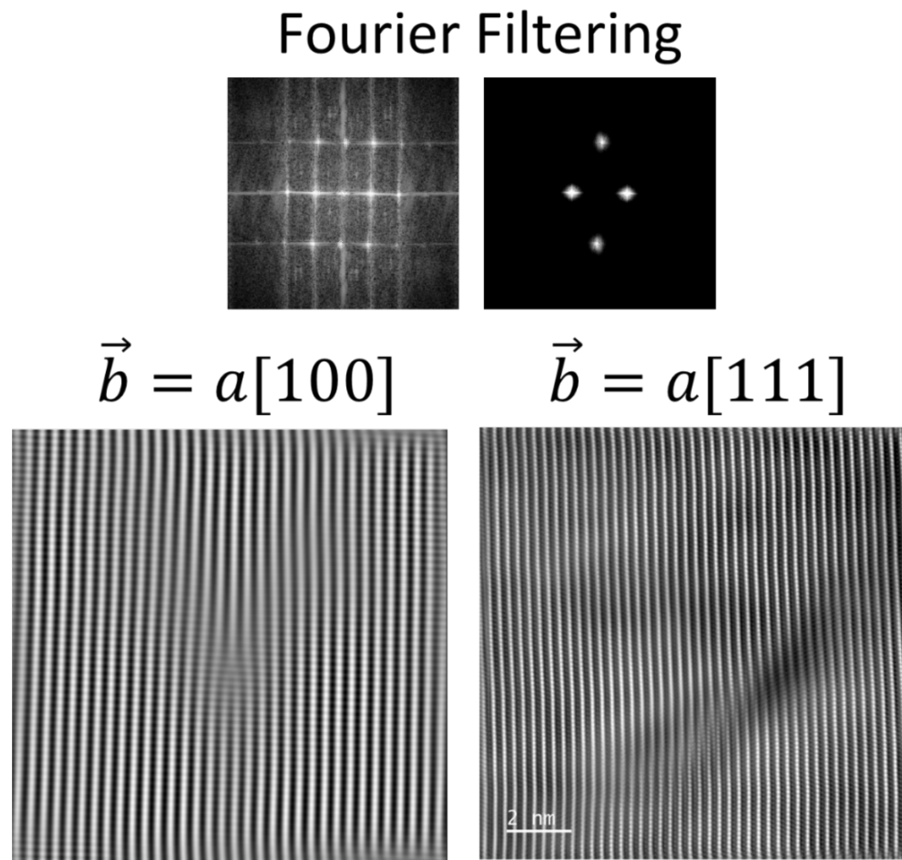

Figure 10-22: Upper images are FFT and masked FFT <200> reflection. The lower left image is a Fourier filter image of a[100] type misfit edge dislocation, and the lower right image is a[111] misfit screw dislocation in an FeRh film, shown in Figure 10-21.

10.5 Geometric Phase Analysis (GPA)

Geometric Phase Analysis (GPA) is a technique for quantifying strain fields around dislocations using HRSTEM or HRTEM images and the observed lattice distortions and atomic displacements around dislocations. The application of GPA to dislocations offers key insights into their influence on material behavior. For example, it allows visualization of the displacement fields caused by edge, screw, or mixed dislocations and enables detailed mapping of lattice rotations and distortions near the dislocation core. This capability is critical for studying how dislocations interact with external stresses and other defects. GPA's nanometer-scale resolution and non-invasive nature make it ideal for investigating a variety of materials, including metals, ceramics, and semiconductors, as well as emerging nanostructures. However, the accuracy of the GPA approach depends heavily on the quality of HRTEM images and the proper selection of diffraction spots, as overlapping strain fields or sample preparation artifacts can complicate analysis.

GPA provides a quantitative approach to mapping strain (ε) and displacement (u) fields around dislocations by analyzing high-resolution transmission electron microscopy (HRTEM) images in reciprocal space. Dislocations such as screw and edge types induce distinct displacement fields that can be extracted using Fourier transform methods, providing a quantitative understanding of the local strain tensor components $\left(u_{xx}, u_{yy}, u_{xy}\right)$ and lattice rotations around dislocations.

Figure 10-23 shows an example of the GPA method. It is essential to capture high-quality HRTEM images of the crystal region containing the dislocation(s), e.g., Figure 10-23 a. Those images are converted from real space to reciprocal space using a 2D Fourier transform, which generates a diffractogram (not actual diffraction patterns) with spots corresponding to lattice periodicity (see inset image of Figure xx a). Then, specific diffraction spots ($\vec{g}$) related to the lattice planes of interest are selected and masked, similar to Fourier filtering, used to better image the dislocation core, e.g., Figure 10-23 b and $\vec{\boldsymbol{g}}(\boldsymbol{x},\boldsymbol{y}) = g_x\hat{x}+g_y\hat{y}$. The geometrical phase, $\phi(r)$, associated with those reciprocal lattice frequencies can be extracted, considering that:

$$\phi(\boldsymbol{r}) = \vec{\boldsymbol{g}} \cdot \vec{\boldsymbol{u}}(\boldsymbol{r}) \qquad 10.23$$

where $\vec{\boldsymbol{u}}(\boldsymbol{r}) = (u_x+u_y)$ is the displacement field in real space. Displacements are measured by calculating the 'local' Fourier components of the lattice fringe, as shown in Figure 10-23b. In this formulation, the intensity in an image, $\boldsymbol{I}(\boldsymbol{r})$, is written as:

$$\boldsymbol{I}(\boldsymbol{r}) = \sum_{\boldsymbol{g}} \boldsymbol{I}_{\boldsymbol{g}}\,(\boldsymbol{r})\boldsymbol{e}^{2\pi i\boldsymbol{g}\cdot\boldsymbol{r}} \qquad 10.24$$

where $\vec{g}$ are the reciprocal lattice vectors describing the undistorted lattice. The local Fourier components are obtained by filtering in Fourier space and have an amplitude and phase of,

$$I_g(\boldsymbol{r}) = A_g(\boldsymbol{r})e^{\boldsymbol{i}P_g(\boldsymbol{r})} \qquad 10.25$$

where the amplitude, $A_g(\boldsymbol{r})$, describes the local contrast of the fringes and the phase, $P_g(\boldsymbol{r})$, their position. The phase is related simply to the displacement field $\vec{\boldsymbol{u}}(\boldsymbol{r})$ by the following equation,

$$P_g(\boldsymbol{r}) = -2\pi\vec{\boldsymbol{g}}\cdot\vec{\boldsymbol{u}}(\boldsymbol{r}) \qquad 10.26$$

and by measuring two phase images, $P_{g1}(\boldsymbol{r}) and\ P_{g2}(\boldsymbol{r})$, and by extracting their amplitude and phase, the two-dimensional displacement field can be determined,

$$\vec{\boldsymbol{u}}(\boldsymbol{r}) = -\frac{\boldsymbol{1}}{\boldsymbol{2\pi}}[P_{g1}(\boldsymbol{r})a_1+ P_{g2}(\boldsymbol{r})a_2] \qquad 10.27$$

Here $a_1\ and\ a_2$ are the basis vectors for the lattice in real space corresponding to the reciprocal lattice defined by g_1 and g_2. The strain components are obtained by differentiating the displacement fields.

For a screw dislocation with a Burgers vector $\vec{b}$ parallel to its line vector $\vec{\xi}$ along z:

- The displacement field $u_z(x,y)$ is rotationally symmetric about the dislocation core.
- Strain is distributed tangentially around the dislocation line.

The strain tensor components include,

$$u_{zx} = \frac{\partial u_z}{\partial x}, u_{xy} = \frac{\partial u_z}{\partial y}$$

For an edge dislocation with a Burgers vector $\vec{b}$ perpendicular to its line vector $\vec{\xi}$ along x:

- The $u_{xx}(x,y)\ and\ u_{xy}(x,y)$ component dominates.

- Strain fields are concentrated near the dislocation line, with tensile strain above and compressive strain below.

The strain tensor components for an edge dislocation are:

$$u_{xx} = \frac{\partial u_x}{\partial x}, u_{xy} = \frac{\partial u_x}{\partial y}, u_{yy} = 0$$

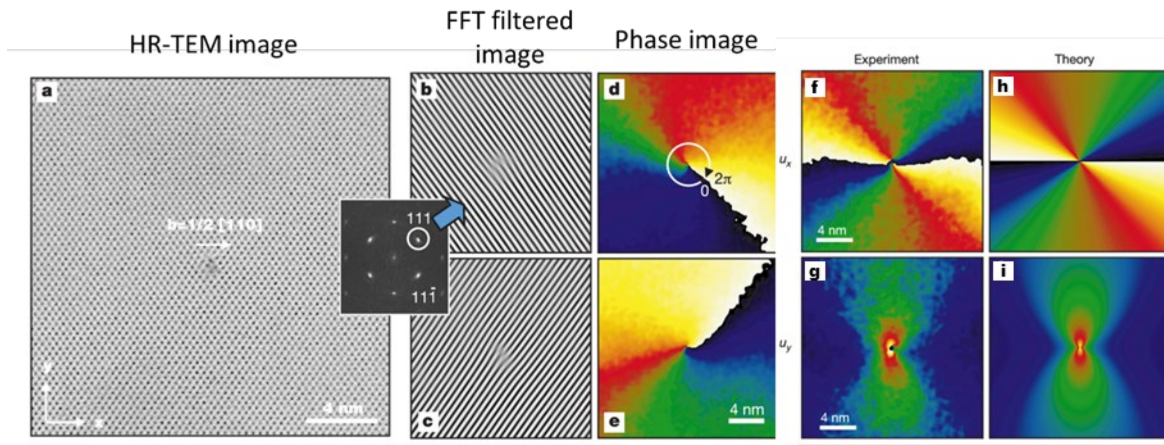

Figure 10-23: a) HRTEM image, b) and c) are Fourier filtered images using the reciprocal lattice spots circled in the inset FFT diffractogram, d) and e) associated phase maps, f) ***Displacement Map showing*** *how atomic planes are shifted around the dislocation, g)* ***Strain Maps*** *highlighting regions of tensile, compressive, and shear strain, h) and i) are theoretical calculations of f) and g)*

Beyond the quantitative analysis of "static" HRSTEM dislocation imaging, GPA is often complemented by other techniques for more comprehensive insights. In-situ TEM, for example, enables real-time observation of dislocation behavior under external stimuli, while molecular dynamics simulations and finite element methods provide theoretical models for comparison. Machine learning methods are increasingly used to automate GPA workflows, enhancing efficiency and consistency. As a versatile tool for materials characterization, GPA is invaluable for optimizing mechanical properties in advanced materials, improving electronic device performance, and investigating defect behavior in low-dimensional systems.

Bibliography

[1] Williams, D. B., & Carter, C. B. (2009). Transmission Electron Microscopy: A Textbook for Materials Science. Springer.

[2] Hirsch, P. B., Howie, A., Nicholson, R. B., Pashley, D. W., & Whelan, M. J. (1965). Electron Microscopy of Thin Crystals. Butterworths.

[3] Humphreys, F. J., & Hatherly, M. (2004). "Recrystallization and Related Annealing Phenomena. Pergamon.